Microwave-assisted synthesis of N/S-doped CNC/SnO2 nanocomposite as a promising catalyst for oxygen reduction in alkaline media

Original
Microwave-assisted synthesis of N/S-doped CNC/SnO2 nanocomposite as a promising catalyst for oxygen reduction in alkaline media / Gianola, G., Garino, N., Bartoli, M., Sacco, A., Pirri, C.F., Zeng, Juqin.. - In: MATERIALS CHEMISTRY AND PHYSICS. - ISSN 0254-0584. - 308:(2023). [10.1016/j.matchemphys.2023.128205]

Publisher:
Elsevier

Published
DOI:10.1016/j.matchemphys.2023.128205

Materials Chemistry and Physics 308 (2023) 128205

Contents lists available at ScienceDirect

Materials Chemistry and Physics

journal homepage: www.elsevier.com/locate/matchemphys

Microwave-assisted synthesis of N/S-doped CNC/SnO_2 nanocomposite as a promising catalyst for oxygen reduction in alkaline media

Giulia Gianola [a,b,*,1], Nadia Garino [a,b,1], Mattia Bartoli [a,c,**], Adriano Sacco [a], Candido F. Pirri [a,b], Juqin Zeng [a,b]

[a] Center for Sustainable Future Technologies @Polito, Istituto Italiano di Tecnologia, Via Livorno 60, 10144, Torino, Italy
[b] Department of Applied Science and Technology, Politecnico di Torino, Corso Duca degli Abruzzi 24, 10129, Torino, Italy
[c] Consorzio Interuniversitario Nazionale per la Scienza e Tecnologia dei Materiali (INSTM), Via G. Giusti 9, 50121, Florence, Italy

HIGHLIGHTS

- Development of tailored carbonized cellulose nanocrystals ORR catalyst.
- Evaluation of synergistic effects of the dopants and SnO_2 nanocrystals in modifying the catalytic performance.
- Prove that co-doping in carbon lattice creates additional active centers that boosted tin particles activity.

GRAPHICAL ABSTRACT

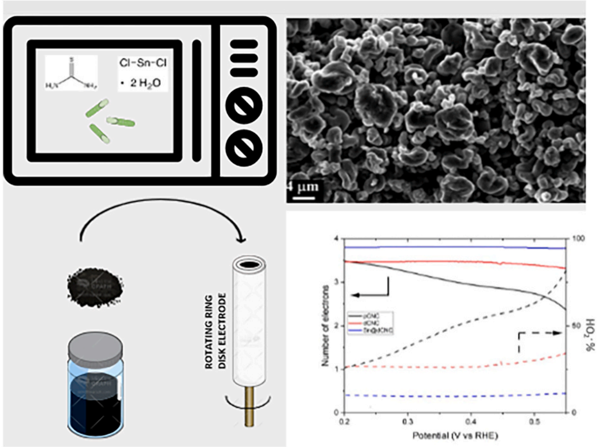

ARTICLE INFO

Keywords:
Heteroatom doping
Cellulose nano crystals
Tin oxide
Oxygen reduction reaction
Microwave

ABSTRACT

In this study, we report an all-green approach for the synthesis of novel catalysts for oxygen reduction reaction (ORR) via a simple two-step procedure. In particular, conductive cellulose nanocrystals (CNCs) were obtained via pyrolysis, and a successive microwave-assisted hydrothermal process was employed to activate the carbon lattice by introducing sulfur (S) and nitrogen (N) dopants, and to decorate the surface with tin oxide (SnO_2) nanocrystals.

The successful synthesis of N/S-doped CNC/SnO_2 nanocomposite was confirmed by X-ray Photoelectron Spectroscopy analysis, Energy Dispersive X-ray microanalysis, X-ray Diffraction and Field Emission Scanning Electron Microscopy. The synergistic effects of the dopants and SnO_2 nanocrystals in modifying the catalytic performance were proved by various electrochemical characterizations. Particularly, the nanocomposite material

---

* Corresponding author. Center for Sustainable Future Technologies @Polito, Istituto Italiano di Tecnologia, Via Livorno 60, 10144, Torino, Italy.
** Corresponding author. Center for Sustainable Future Technologies @Polito, Istituto Italiano di Tecnologia, Via Livorno 60, 10144, Torino, Italy.
E-mail addresses: giulia.gianola@iit.it (G. Gianola), mattia.bartoli@iit.it (M. Bartoli).

[1] These authors contributed equally.

https://doi.org/10.1016/j.matchemphys.2023.128205
Received 31 March 2023; Received in revised form 24 June 2023; Accepted 17 July 2023
Available online 22 July 2023

reaches remarkable catalytic performance towards the ORR, close to the Pt/C benchmark, in alkaline environment, showing promising potential to be implemented in alkaline fuel cell and metal-air battery applications.

1. Introduction

In the last decades, the increasing demand for renewable energy and the attention on global warming issues have determined growing efforts from the scientific community in the search of novel and effective technological solutions alternatives to fossil fuels and to mature a conscious usage of raw materials [1]. In this scenario, low emission and high efficiency technologies for energy conversion and storage, such as fuel cell and metal-air battery devices, can be considered promising systems for a more sustainable future [2,3]. Unfortunately, the large-scale commercialization of these devices is nowadays limited by different factors that affect their huge potential. In detail, a key point is represented by the sluggish kinetics of cathodic oxygen reduction reaction (ORR). To overcome the high kinetic barriers of this process, a dedicated catalyst is needed to reduce the overpotential and increase the reaction rate. Particularly, for fuel cell application, another fundamental goal is to hinder the two-electron pathway, which is in competition with the direct four-electron one, and in this way to increase the system efficiency with the direct conversion of oxygen into water. In addition, this drastically reduces the production of hydrogen peroxide, which is well-known corrosive and poisoning molecule for fuel cell components [4].

Up to now, noble metals (in particular platinum) supported on carbon substrates with high surface areas are considered as benchmark catalysts for ORR [5], but the very high cost and scarce availability of such materials drastically reduce the practical application of fuel cells. Hence, great efforts have been made to develop inexpensive but efficient noble metal-free catalysts by looking in particular at highly available materials such as metal oxides [6–11]. In particular, carbon doped with heteroatoms and tailored with tin oxides proved to be a winning strategy, showing good selectivity towards the four-electron pathway, good long-term operational stability, very good chemical stability, high mass transport and electric conductivity of carbon-based materials [12–14]. On the other hand, the recycling and recovery of materials from wastes [15] or biomass, like biochar, have been attracting attention and are considered as promising strategies for a greener circular economy [16,17].

Recently the carbon-based materials derived from biomass have demonstrated very promising implementation in energy storage and conversion systems [18,19] even though from unusual and exotic sources [20]. The increased accountability for environmental preservation has boosted up the use and development of waste streams and bioderived valorization in the energy storage field. Of particular interest, lignocellulosic biomass represents one of the most abundant carbon source from which it is possible to obtain different kinds of carbon structure like fibers, crystalline or hierarchical ones [21–23], producing hard carbon widely used for applications in sodium ions batteries [24], supercapacitors [25] and fuel cells [26].

In this study we considered cellulose nanocrystals (CNCs) as starting point for the preparation of conductive carbon lattice via pyrolysis [27,28]. This is because the pristine CNCs present very good aspect ratio [29] and result to be an ideal precursor for conductive lattice with promising electrochemical properties [30]. Subsequently, the as-prepared biochar was activated by introducing sulphur and nitrogen co-dopants with simultaneous tin oxide decoration on the carbon surface by employing a fast and green microwave-assisted hydrothermal process.

It is well-known that the introduction of heteroatoms (e.g. N, P, B, S) in a carbon lattice can strongly affect the electrochemical properties of carbon-based catalysts, showing enhanced selectivity towards the four-electron ORR path [31,32]. In this work, we used both nitrogen and sulphur atoms due to their proved capability of introducing a large number of active centers for a better oxygen adsorption [33] and lattice defects enhancing the overall ORR catalytic activity [34]. In addition, tin oxide, being a good candidate catalyst for ORR as already reported in the literature [35–37], shows remarkable electrocatalytic activity towards ORR when it is anchored on the doped carbon. All the prepared samples were systematically investigated in their catalytic activities towards ORR through different electrochemical techniques. Thanks to the co-doping with sulphur and nitrogen together with tin oxide nanoparticles decoration, the nanocomposite catalyst demonstrated a notable ORR activity, and can be considered a promising low-cost and green alternative to platinum-based catalysts.

2. Experimental

2.1. Conductive CNCs synthesis

Neat CNCs were purchased from Alberta-Pacific Forest Industries (Batch COMP170823-H) and used as received without any purification. Neat CNCs were pyrolyzed using a vertical furnace and a quartz reactor (heating rate: 15 °C/min) and kept at 400 °C for 30 min in nitrogen atmosphere. Pyrolyzed CNC were annealed by using a vacuum electric furnace (Pro.Ba., Cambiano, Italy) under Argon atmosphere (99.99% purity, controlled pressure 550 mbar) using a heating rate of 150 °C/h, a dwell at the maximum temperature of up to 1500 °C for 30 min and a cooling to room temperature with the same thermal gradient used for heating accordingly with procedure reported by Giorcelli et al. [38] recovering a carbonaceous material named pCNC.

2.2. CNCs doping and functionalization

All the chemicals were used as purchased without further purification. The co-doped dCNC and tin oxide nanocomposite (Sn@dCNC) were prepared by following the synthesis procedure described hereafter. In a microwave 100 mL Teflon reactor equipped with pressure and temperature probes (Milestone FlexyWave, Milestone Inc, Shelton, Connecticut), 350 mg of pCNC were added to 30 mL DI water, with 140 mg of thiourea (Sigma-Aldrich). Then, 175 mg of pCNC of $SnCl_2•2H_2O$ (Sigma-Aldrich) were added and dissolved in the as-prepared mixture by using an ultrasonic bath (Elmasonic S, Elma Schmidbauer GmbH, Singen, Germany) for about 30 min in order to obtain a homogeneous dispersion. Subsequently, the resulting precursor mixture slurry was irradiated for 15 min at 180 °C (800 W maximum). The reactor was then cooled down to room temperature. The resultant suspension was then collected after the removal of the surnatant, and the resulting powder was washed with DI water and then dried at 60 °C overnight. The sample without SnO_2 NPs (the already mentioned dCNC) was prepared with the same procedure without the addition of tin precursor.

2.3. Physical and electrochemical characterization

Morphological characteristics of the samples were obtained through Field Emission Scanning Electron Microscopy (FESEM Supra 40, Zeiss, Oberkochen, Germany) equipped with a Si(Li)detector (Oxford Instruments, Abington, UK) for energy-dispersive X-ray spectroscopy.

X-ray diffraction (XRD) patterns of the samples were acquired with a PANalytical X'Pert Pro diffractometer (Cu-Kα radiation, 40 kV and 30 mA) equipped with an X'Celerator detector.

The material chemical composition was investigated by using a PHI 5000 Versaprobe Scanning X-ray Photoelectron Spectrometer (monochromatic Al K-alpha X-ray source with 1486.6 eV energy). A spot size of

100 μm was used in order to collect the photoelectron signal for both the high resolution (HR) and the survey spectra. Different pass energy values were exploited: 187.85 eV for survey spectra and 23.5 eV for HR peaks. All samples were analyzed with a combined electron and argon ion gun neutralizer system, in order to reduce the charging effect during the measurements. The semi-quantitative atomic compositions and deconvolution spectra were obtained using Multipak 9.6 dedicated software. All core-level peak energies were referenced to C1s peak at 284.5 eV and the background contribution in HR scans was subtracted by means of a Shirley function.

Raman spectra were collected using a Renishaw inVia (H43662 model, Gloucestershire, UK) equipped with a green laser line (514 nm) with a 50×objective. Raman spectra were recorded in the range from 500 cm^{-1} to 3500 cm^{-1}. Deconvolution of Raman spectra was performed with a homemade software developed using Matlab® (version R2020a) according to the procedure proposed by Tagliaferro et al. [39].

All the electrochemical characterizations were performed at room temperature with a CHI760E electrochemical workstation and ALS RRDE-3A rotating ring disk electrode apparatus. The catalyst samples were deposited onto a glassy carbon disk/Pt ring working electrode (electrode area 0.1256 cm^2) following the procedure reported in Garino et al. [40]. A Pt wire was used as counter electrode and Ag/AgCl was used as reference electrode. Unless otherwise specified, all the measurements were carried out in 3-electrodes configuration (disk/reference/counter electrodes) in oxygen-saturated 0.1 M KOH aqueous electrolytic solution with 2500 RPM rotation speed. All the potentials are always referred to the reversible hydrogen electrode (RHE).

Cyclic voltammetry (CV) curves were acquired from 0.18 V to 1.18 V with a scan rate of 10 mV/s in O_2- and N_2- saturated electrolytic solution. Rotating disk electrode (RDE) tests were carried out through linear sweep voltammetry (LSV) in the potential range 0.18 V–1.18 V with a scan rate of 5 mV/s and variable rotation speed in the range 400–2500 RPM. Rotating ring-disk electrode (RRDE) measurements were carried out through LSV in 4-electrodes configuration (disk/ring/reference/counter electrodes) by scanning the disk electrode from 0.18 V to 1.18 V (scan rate 5 mV/s) and fixing the ring potential at 1.18 V. EIS measurements were performed at fixed 0.68 V potential, with an AC signal of 10 mV amplitude and 10^0–10^6 Hz frequency range. Finally, chronoamperometry (CA) curves were acquired at fixed 0.68 V potential.

3. Results and discussion

3.1. Morphological analysis

Neat CNC present several shapes based on the production route used for their fabrication [41]. We used neat CNC produced by a hydrolytic and enzymatic route as reported by Beyene et al. [42] with a deformed discoidal shape [27]. Nevertheless, neat CNCs are not compatible with electrochemical uses due to the lack of conductivity and the high oxygen carbon ratio. Accordingly, we carbonized them obtaining carbon microspheres as described by Bartoli et al. [27]. Common pyrolytic temperatures barely match the optimal carbonization degree and carbon crystallinity of high-performance carbon such as graphene and carbon nanotubes. Accordingly, we annealed the pyrolyzed CNC at 1500 °C producing a high crystalline carbon material further discuss in the next sections. A preliminary morphology investigation of carbonized and tailored CNC is shown in Supporting information Fig. S1.

As shown in Fig. S1a, pCNC is characterized by a centered deformed discoidal structure with a diameter ranging from around 5 μm up to 20 μm with a thickness ranging from 2 up to 10 μm. A close view of the surface of pCNC (Fig. S1b) enlightens the presence of a homogenous texture composed by hemispheres with average radii of up to 300 nm. These structures were formed during the pyrolytic conversion due to the carbonization of the volatile organic matter released from the inner core of the particles that was converted into carbon prior to boiling up away from the reaction environment. Morphology of dCNC is not particularly affected by the doping process with a retention of the particle size (Fig. S1c). Nevertheless, the microwave tailoring process removes the hemispheres from the carbon particle surface as shown in Fig. S1d. CNC particle size is also preserved in the Sn@dCNC sample (Fig. S1e), and as clearly shown in Fig. S1f tin oxide nanoparticles are present on the carbonized CNC surface. As shown in the red circled highlight of Fig. S1f, tin oxide nanoparticles display an average size of around 10–20 nm with a polyhedral morphology.

As shown by the EDX mapping reported in Fig. 1, the heteroatoms (sulphur and nitrogen) distribution is quite homogenous while oxygen and tin show the formation of small clusters in agreement with the morphology of the tin nanoparticles observed in Fig. S1f. According to EDX elemental analysis, the amounts of nitrogen and sulphur are 0.6 wt % and 1.0 wt% respectively, suggesting a partial surface modification of pCNC without compromising the carbonaceous core (carbon content of 77.5 wt%).

3.2. Spectroscopical analysis

A detailed Raman analysis was carried out on pCNC, dCNC and Sn@dCNC for the evaluation of carbon organization [43]. The output of fitted spectra (Fig. S2) was used to evaluate the I_D/I_G ratio and the average length of graphitic cluster diameter (L_α) accordingly with the procedure established by Tuinstra and Koenig [44] as summarized in Fig. 2.

The I_D/I_G ratio of pCNC is 0.7 and its Raman spectrum (Fig. S2a) shows a well resolved D and G region and a quite structured 2D region, suggesting a highly ordered graphitic like carbon [45,46]. This is supported by the large size of L_α up to 58 Å. The microwave doping and functionalization procedure increments the disorganization of the carbonaceous structures, increasing the I_D/I_G ratio up to 1.0 and 1.4, respectively. This could facilitate a better absorption of oxygen molecule on the carbon surface and significantly reduce the activation barrier of chemisorbed oxygen atoms, as widely studied not only from a theoretical point of view [47,48]. On the other side, L_α shows an opposite trend, with a significant decrement of graphitic crystalline size down to 42 Å and 30 Å for dCNC and Sn@dCNC, respectively. The trends reported in Fig. 2 suggest that the incorporation or deposition of heteroatoms (see Table 1) damaged the carbon lattice structure with an appreciable increment of disorganization.

A more detailed evaluation of the carbonized CNCs has been done through XPS spectra reported in Fig. 3 (see Supporting information Fig. S3 for the survey spectra) and from their outputs summarized in Table 2.

The high-resolution C 1s spectrum of pCNC (Fig. 3a) shows a very high concentration of C sp^2 (284.6 eV) up to 85.9% with the presence of traces of oxidation compatible with their exposition. Traces of C sp^3 (283.6 eV) are reasonably due to edge defects and surface passivation accordingly with the C-X component detected at 285.9 eV. The elemental composition includes traces of fluorine and of silicon due to the impurity on the CNC material that were removed in the production of both dCNC and Sn@pCNC. Additionally, dCNC and Sn@dCNC show no trace of silicon due to their removal during the hydrothermal process (Supporting information Table S1). As shown in Fig. 3f, dCNC shows a decrement of C sp^2 percentage down to 68.5% with an increment of C-X up to 28.0% due to the insertion of both nitrogen and sulphur atoms. The treatment in water under microwave irradiation for the production of Sn@dCNC induced a further oxidation of the surface of carbonized CNCs with an increment of C═O up to 15.6 and massive presence of C═O (287.4 eV) up to 69.2% of the total oxygen functionalities. Nitrogen atoms have been included into the carbonaceous structure mainly as amines functionalities (399.3 eV) [49] up to 76.4% and aromatic species (pyrrolic N5, graphitic NQ). As shown in Fig. 3i, sulphur is included mainly as thiol functions (164.7 eV) up to 81.4% able to stabilize the tin oxide particles but also trace of sulphonyl residues (168.8 eV) have been

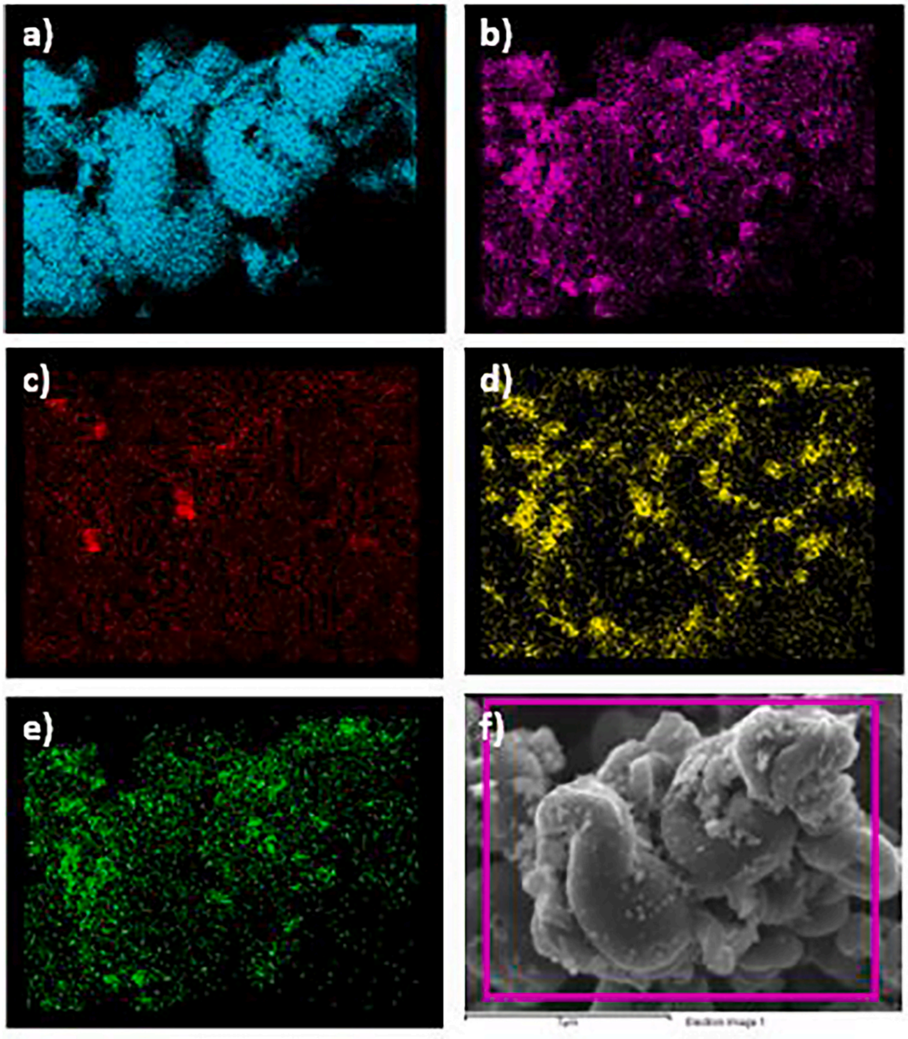

Fig. 1. EDX mapping of Sn@dCNC of a) carbon, b) oxygen, c) sulphur, d) nitrogen and e) tin.

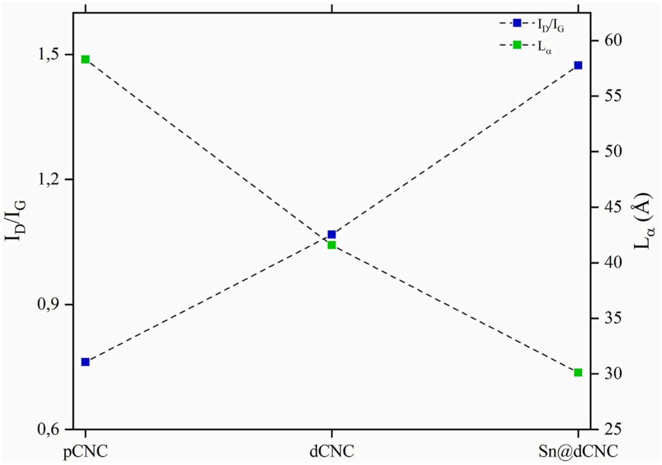

Fig. 2. Comparison of the I_D/I_G ratio and L_α trends of pCNC, dCNC and Sn@dCNC.

detected probably formed as consequence of radical oxidative reactions due to the decomposition of thiourea [50].

Sn@dCNC shows a percentage of tin up to 6.8% (Supporting information Table S1) present as SnS ($3d_{3/2}$ 486.9 eV, $3d_{5/2}$ 495.3 eV) and SnO_2 ($3d_{3/2}$ 488.0 eV, $3d_{5/2}$ 486.4 eV) up to 63% and 37% respectively as shown in Fig. 3o. Furthermore, we observed a significant change in the sulphur signal that shows only the presence of thiols (Fig. 3n) and SnS together with a drastically modification of nitrogen spectra (Fig. 3m). Nitrogen shows a drastically decrement of amino functions down to 8.6% while the ratio of N5/NQ (2.48) remains quite close to the one observed for dCNC (2.52) probably due to degradation during the further decoration for tin oxide nanoparticle. Moreover, the percentage of graphite-like nitrogen atoms increases for the Sn@dCNC sample, implying an easier adsorption of oxygen molecules and therefore higher oxygen reduction reaction activity, as reported by Kabir et al. [51].

Table 1
Elemental composition of Sn@dCNC as calculated using EDX technique.

Element	Weight percentage (%)
C	77.5
N	0.6
O	8.5
Na	0.3
S	1.0
Cl	0.3
Sn	11.6

XRD analysis was performed to study the crystalline structure of the Sn@dCNC material. As shown in Fig. 4, the Sn@dCNC sample shows

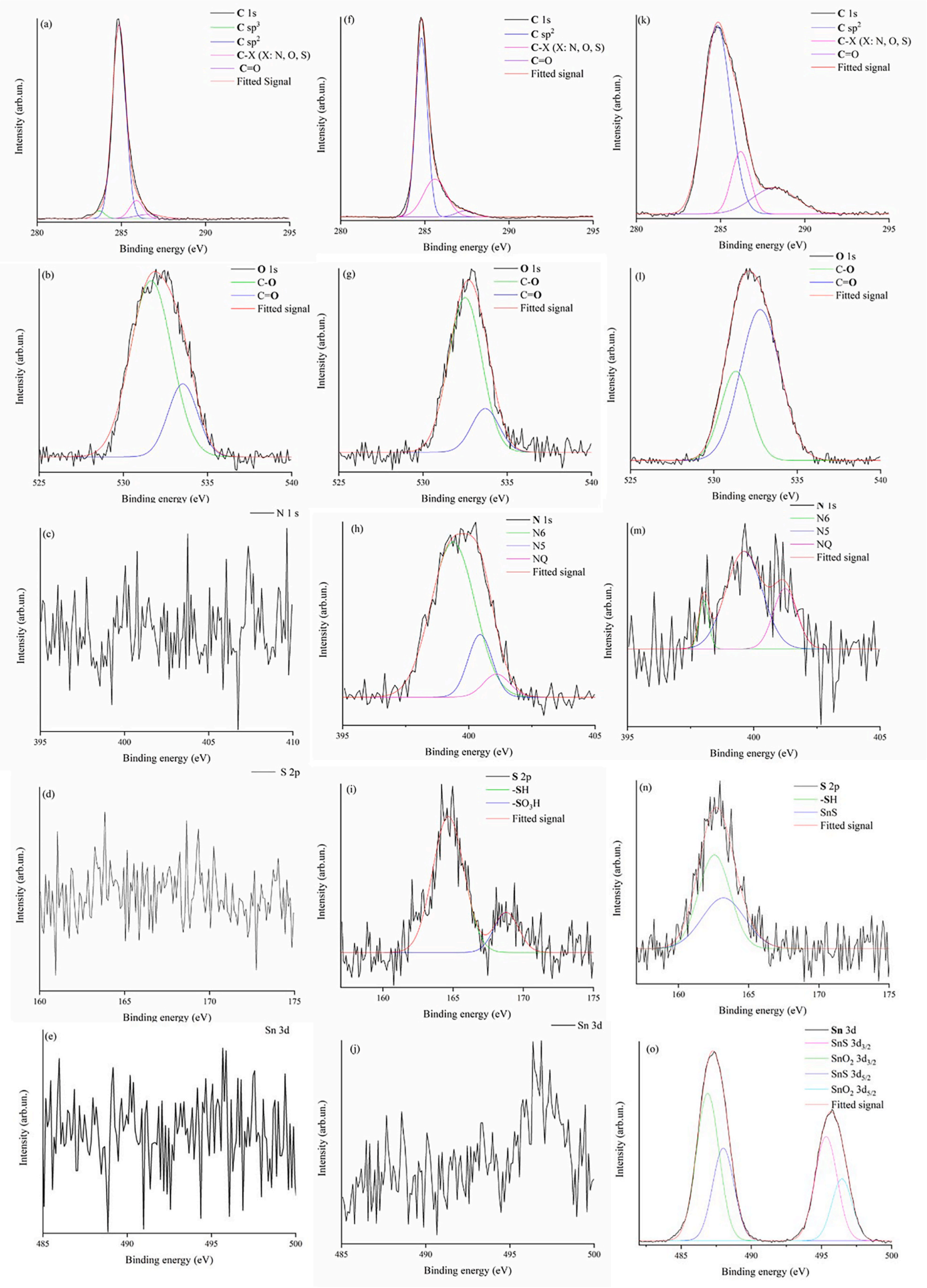

Fig. 3. XPS spectra of a-e) pCNC, f-j) dCNC and k-o) Sn@dCNC. Baselined and fitted signals were reported in black and red respectively. (For interpretation of the references to colour in this figure legend, the reader is referred to the Web version of this article.)

Table 2
XPS functions composition according with fitted spectra reported in Fig. 3.

Sample	Carbon (%)				Oxygen (%)		Nitrogen (%)			Sulphur (%)			Tin (%)	
	C sp^3	C sp^2	*C-X (X: O.N. S)*	C=O	C-O	C=O	$-NH_2$	N5	NQ	-SH	$-SO_3H$	SnS	SnS	SnO2
pCNC	2.7	85.9	8.1	3.3	77.2	22.8	—	—	—	—	—			—
dCNC	—	68.5	28.0	3.5	81.1	18.9	76.4	16.9	6.7	81.4	18.6			—
Sn@dCNC	—	68.8	15.6	15.6	30.8	69.2	8.6	65.1	26.3	58	—	42	63	37

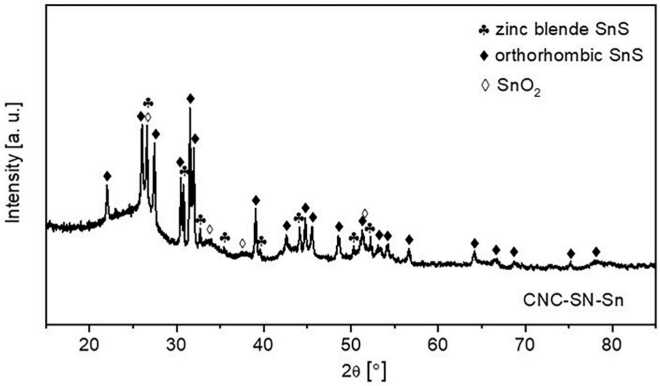

Fig. 4. XRD pattern of Sn@dCNC sample.

broad peaks related to SnO_2 with a tetragonal structure (reference code: 00-041-1445). Well-defined peaks associated with the bulk orthorhombic crystal structure of SnS (reference code: 00-039-0354) and the structure of tetrahedral zinc blende SnS [52]] are also identified. XRD measurement has also been carried out on CNC material for comparison, as shown in Fig. S4. The CNC sample shows a main diffraction peak close to 23.9° (2θ), which is related to the graphitic structure (002) plane and negatively shifted with respect the pure graphite that has a (002) peak at about 26.7° [53]. Due to the contribution of CNC, the XRD pattern of Sn@dCNC shows a broad peak at low 2θ position (<30°), besides the well-defined peaks for orthorhombic and zinc blende SnS and SnO_2 phases.

Concisely, the nanocomposite is composed of Sn-based nanoparticles supported on a doped CNC carbon support. A thorough XPS confirms the doping of CNC carbon with nitrogen and sulphur, which could contribute to the activation of oxygen by promoting its adsorption on the surface. The coexistence of SnO_2 and SnS is revealed by XPS and XRD analyses. This outcome is reasonable, since the precursor solution contains $SnCl_2$ and thiourea that are also well-known precursors for SnS synthesis. Both Sn species are reported as good electrocataysts for the ORR in literature. This work will conduct a complete electrochemical investigation on the synthesized nanocomposite material in order to evaluate its potential in practical applications based on its already known appreciable characteristics such as low-cost precursors, waste recovery feature and environmentally friendly synthesis procedure.

3.3. *Electrochemical characterization*

The catalytic activity of the functionalized CNC samples was assessed through different electrochemical techniques, as reported here below.

Fig. 5 shows the CV curves acquired in both N_2- and O_2-saturated electrolytic solutions. All samples exhibit a reduction peak in the cathodic scan at potentials in the range of 0.5–0.6 V, when the curve is acquired in an O_2-saturated KOH electrolyte. The peak disappears in the N_2-saturated solution, confirming the capability of the CNC-based materials to catalyze the ORR, even when no doping or decoration occurs.

It is interesting to notice that the activity of pCNC results to be slightly higher with respect to that of dCNC. Because of the annealing process performed at high temperatures on the pCNC material, a high degree of conductivity is guaranteed, as highlighted by the current density achieved in the cyclic voltammogram (Fig. 5a). However, when doping is performed, a lower conductivity is read (Fig. 5b). Heteroatoms are characterized by different sizes and electron negativity with respect to those of carbon atoms, causing a change in the charge distribution and electronic properties of the carbon matrix, which ultimately affects the electrocatalytic activity of the ORR. Adding S and N heteroatoms to pristine CNC implies a more defective crystalline organization of the material, thus resulting in a less ordered graphitic structure. Consequently, the conductivity between different graphitic domains turns out to be less favorable, as results from Raman spectroscopy analysis reported in Fig. 2, and the activity of the dCNC sample appears lower with

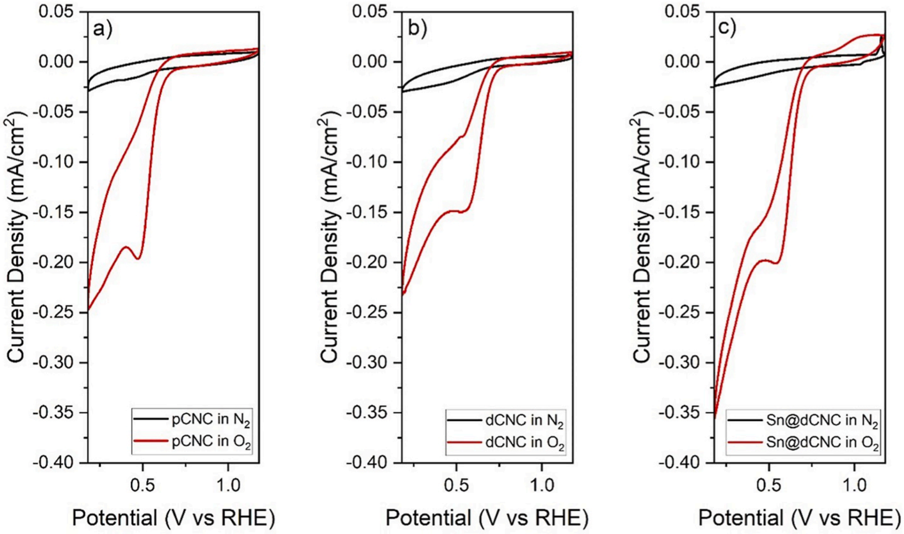

Fig. 5. Cyclic voltammograms of the different catalysts in O_2-saturated and N_2-saturated solutions: a) pCNC b) dCNC c) Sn@dCNC

respect to the non-doped pCNC catalyst. Finally, once the sample is decorated with SnO_2, an improvement in the performances of the catalyst occurs (Fig. 5c), highlighting the beneficial effects of the tin oxide decoration. This can be further appreciated by looking at the higher potential at which oxygen reduction occurs (0.56 V), quite in agreement with other electrocatalysts proposed in the literature for the ORR [8,11,12].

The catalytic pathways of the ORR, namely the direct reduction of molecular oxygen to hydroxide ions (exploiting 4 electrons) and the indirect reduction to peroxide ions (exploiting 2 electrons) [50], were investigated through both RDE and RRDE measurements. By looking at the LSV plots related to the RDE analysis (Fig. S5), it is possible to notice how the catalytic activity increases for increasing rotation rates. When the electrode is rotating, the solution flows from the bulk to the surface, where it is then flushed away parallel to the disk surface. In this way new fresh solution is continuously brought in contact with the electrode surface, increasing the mass diffusion and therefore the amount of oxygen to be reduced, leading to higher limiting current densities. Moreover, from RDE data, it is possible to extrapolate the number of electrons involved in the oxygen reduction reaction thanks to the Koutecky-Levich (KL) plots (Fig. S6). KL plots have been reported in the potential range (0.4–0.6) V vs RHE, range particularly significant because it is the region where the current densities undergo mixed kinetic and mass transfer control. Because of the similar shapes achieved at different potentials, the number of transferred electrons has been computed trough KL slopes only at 0.4 V vs RHE. Both dCNC and Sn@dCNC samples' analysis report a number of electrons equal to 3.9, demonstrating the selectivity of both material towards the 4-electrons reduction pathway. This result can be further demonstrated by Tafel plots. These have been achieved by KL plots computed in the potential range (0.6–0.75) V vs RHE, to consider the kinetic region of the reducing currents. Fig. S7 reports the mass-transfer corrected Tafel plots, where the logarithm of the kinetic currents has been plotted against the selected potentials. As it can be noticed from the plot, both dCNC and Sn@dCNC samples show Tafel slopes which are close to each other. It is possible thus to deduce that similar reaction mechanisms are involved for both samples, as it was already demonstrated by the number of electrons involved in ORR obtained by RDE measurement. For what concerns RRDE measurement, the disk potential is scanned at a fixed rotation rate of 2500 rpm at 1.18 V vs RHE and the currents at both disk and ring electrodes are measured. Results are reported in Fig. S8. To have an efficient catalyst, the disk current must prevail on the ring one, therefore higher values of the disk current are expected. According to the results achieved from the RRDE measurements, all samples exhibit a predominant direct pathway for the ORR in which 4 electrons are involved, implying that the current related to the two electrons ORR peroxide species is low. Both doping and decoration play a role in determining the selectivity of the 4-electron reduction reaction, showing a very small ring current with respect to the pristine sample. However, also, in this case, the defects induced by doping influence the performance of the doped sample, resulting in a slightly lower disk current. On the other hand, the tin oxide decoration results to improve the selectivity of the sample, favoring the direct reduction reaction, as evidenced by the very low ring current. Furthermore, it can be noticed that both heteroatom doping and tin oxide decoration cause a decrease in the ring currents in the region above 0.6 V [Fig. S8b], satisfying the requirement that oxygen reduction proceeds via a complete direct 4-electron pathway at potentials relevant for the fuel cell cathodes. Finally, to quantify the ORR activity, the onset potential is used. Both treated samples exhibited similar onset potentials (0.7 V for dCNC and 0.68 V for Sn@dCNC), while a lower one is achieved for the pCNC sample ($E_{on} = 0.6$ V), meaning that both doping and decoration are beneficial to improve the electrochemical properties.

To further investigate the ORR catalytic performance of the samples, ring current and disk current are then used for the calculation of the number of electrons transferred during the reaction and the consequent percentage of peroxide species accountable for the indirect 2-electrons pathway. By exploiting the following equations (1) and (2), the results reported in Fig. 6 are achieved.

$$n = 4 \times \frac{I_D}{I_D + I_R/N} \tag{1}$$

$$HO_2^- \% = 200 \times \frac{I_R/N}{I_D + I_R/N} \tag{2}$$

Where I_R and I_D are the ring and disk currents, while N is the current collection efficiency of the Platinum ring.

The number of transferred electrons results to be quite stable at higher cathodic potentials, where the electron transfer mechanism is similar in all samples. After ~0.2V, this mechanism is subjected to an evident loss of stability for the pristine sample, implying a lower number of transferred electrons in the reduction reaction and a consequent rise in the peroxide percentage yield. Considering the treated dCNC and Sn@dCNC, the electron transfer mechanism keeps its stability in the given potential window for the reaction. At 0.4V the number of transferred electrons is 3 for pCNC, 3.5 for dCNC, while it rises to 3.8 electrons for the doped and decorated sample, Sn@dCNC. It is important to highlight that this result is in agreement with what reported in the RDE analysis above. On the other hand, the percentage of produced HO_2^- species is very high for the pCNC sample, confirming the poor selectivity of the 4-electron reduction pathway with respect to the doped and decorated samples. The formation of peroxide is as high as about 40% for the dCNC sample, while it definitely decreases for Sn@dCNC, reaching nearly 12%. Since in fuel cell application H_2O_2 production is damaging and the direct 4-electrons mechanism is preferred to get water as the only product, the CNC-based catalyst needs to be functionalized with both doping and decoration to improve its selectivity towards the direct reduction pathway.

To further analyze the performance of the materials under investigation in terms of ORR catalytic activity, electrochemical impedance spectroscopy analysis is performed, and results are reported in Fig. 7.

Generally speaking, the total impedance of an electrochemical system can be attributed to three different processes. The first one involves the charge transport limitation inside the catalyst at high frequencies. The second one, at intermediate frequencies, is associated with the charge transfer at the catalyst/electrolyte interface. The last one, at low frequencies, is related to the diffusion of species to the catalyst/electrolyte interface. As can be noticed by the Nyquist plot in Fig. 7, in this work only one single arc appears, corresponding to a single time

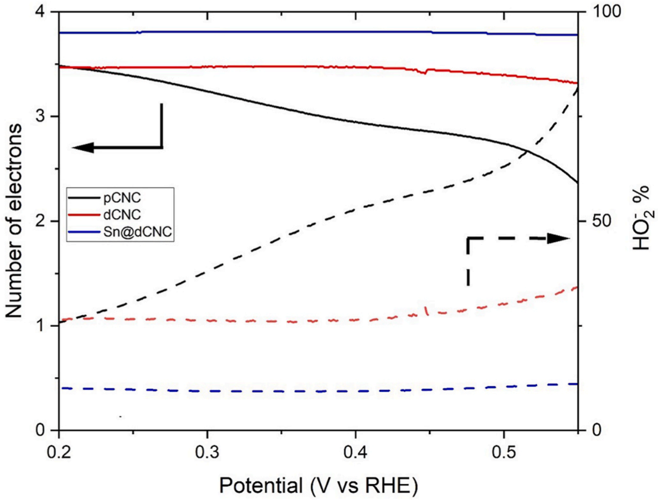

Fig. 6. Comparison of electron transfer number (left axis) and peroxide percentage (right axis) evaluated from RRDE measurements of the different catalyst samples at 2500 RPM rotation speed and different potentials.

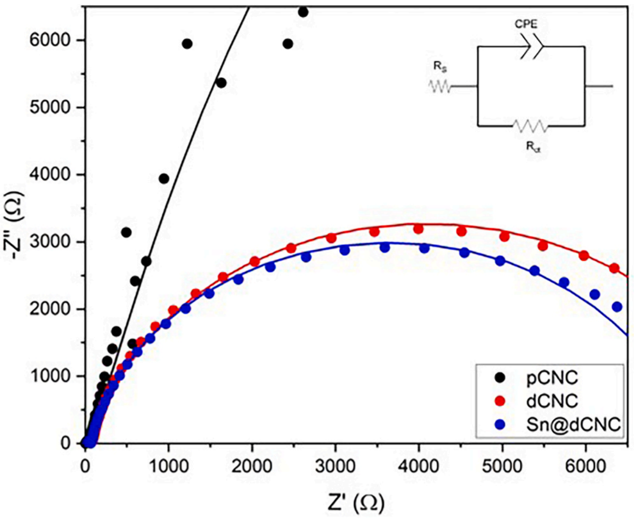

Fig. 7. Nyquist plot of the impedance of the different samples measured at 2500 rpm rotating speed and 0.68 V. The points are experimental data while the continuous lines are the curves obtained from a fitting procedure using the equivalent circuit shown as an inset. The other inset reports a zoom of the curves in the high-medium frequency range.

constant related to the impedance at the electrode/electrolyte interface. Because of the high impact of this process, the one occurring at high frequencies is hidden. Finally, no phenomena can be observed in the low frequency range since the measurement was cut at 1 Hz. The inset shows the equivalent circuit used to model the processes related to the total impedance, known as Randles' circuit [51]. R_s is the series resistance, which takes into account the electrolyte conductivity. The parallel element is introduced because the current flowing through the electrode interface is mainly due by two contributions, one associated to the faradaic process and the other related to the double-layer charging. Therefore, R_{ct} is the charge transfer resistance related to electron transfer at the catalyst/electrolyte interface and the constant phase element [52], which models the double layer capacitance Q_{dl}, refers to the charge accumulation at the solid/liquid interface. To better quantify the impedance spectra, this equivalent circuit is used to fit the experimental data. The fitted data are superimposed to the experimental curves and a good matching between measured and calculated data can be achieved, confirming the good choice of the equivalent circuit for the fitting analysis.

In accordance with RRDE measurements reported before, it is possible to confirm the performance in terms of activity. In particular, we can observe how the charge transfer resistance decreases for the treated samples. At first, doping by heteroatoms only, implies a lower resistance at the electrode/electrolyte interface, which is further reduced in the decorated sample. Tin oxide decoration provides more active sites such that the electron transfer at the catalyst/solution interface improves. From the fitting procedure, it is possible to obtain the values of the charge transfer resistance for all samples, which can be directly related to the catalytic properties of the materials. As expected, the largest value is achieved for the pristine sample pCNC (68777 Ω), while a decrease is noticed for the dCNC sample (8585 Ω) and a further lowering of the charge transfer resistance is achieved for the Sn@dCNC material (7447 Ω), in accordance with all measurements described above.

Finally, the durability of the samples was investigated with a chronoamperometry (CA) measurement for more than 3 h, in Fig. 8.

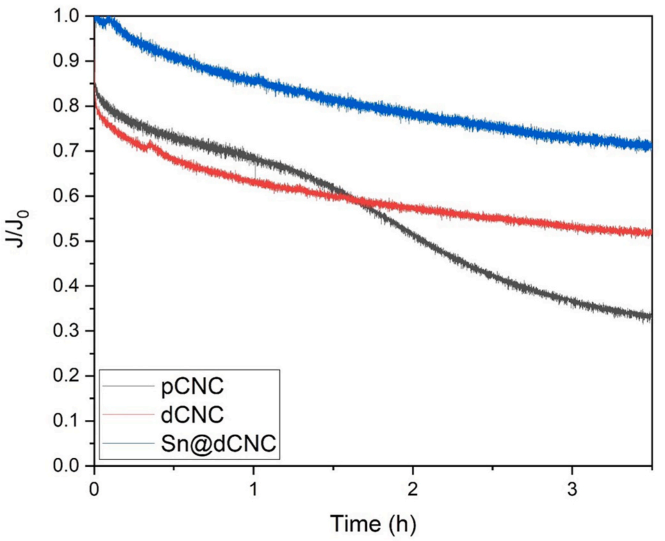

Fig. 8. Chronoamperometric curves of samples measured at 0.68 V vs RHE with 2500 RPM rotation speed and normalized with respect to the initial current value.

From the data achieved by the CA test, it is possible to notice that the oxygen reduction currents decrease with time for all samples. The initial loss of stability may come from capacitive effects, like the charge/discharge process in the double layer. This phenomenon occurs in the first seconds of testing, and it is evident for pCNC and dCNC materials, which lose almost 15% and 20% of their initial normalized current density, respectively. The long-term losses, slower than the initial ones, may be related to faradaic effects, and linked both to a decrease of the specific area or loss of the active material on the electrode. Nonetheless, the advantages of doping and tin oxide decoration can be appreciated. For the pristine sample, the current decrease is more evident, confirming a poor stability of the pure pCNC material (~65% losses). In particular, an important loss of stability occurs during the second hour of testing, where a drop of almost 30% of the current density with respect to that one measured in the first hour can be noticed. This leakage can be likely attributed to an important degradation of the catalyst material occurred. This phenomenon could be caused by the action of the electric field on the catalyst surface or by the disturbing effect of the oxygen bubbles on the material active area, both leading to a possible detachment of the catalyst. On the other hand, for dCNC and Sn@dCNC samples, a slower decrease with time is achieved, corresponding to ~45% and ~25% respectively, thus witnessing the improved catalytic performances of dCNC and the further enhanced one of the decorated material.

4. Biochar based systems: a brief literature comparison

As well-known, one of the most significative additional tools employed for the estimation of catalytic efficiency of ORR materials is the onset potential. This value is not defined universally, since its meaning may vary from paper to paper. As reported by Khotseng et al. [53], the E_{onset} is the potential corresponding to 5% of the diffusion-limited current density, while others define it as the potential where the actual current density approaches the threshold value of 0.1 mA/cm^2 [54]. Therefore, it is not always trivial to compare literature results according to this activity-estimation parameter. In this case, the first method was used to determine the onset potential, and, to better understand the selectivity of literature's materials towards the 4-electrons ORR pathway, the number of transferred electrons during the reduction reaction is reported in Table 3 for biochar-based materials tested in 0.1 M KOH electrolyte.

As an example, cerium oxide nanoparticles are widely used to tailor biochar electrocatalysts, playing an important role in the ORR. Biochar-based materials decorated with rare-earth metal oxide nanostructure, can compete with Pt/C catalyst [55,56]. Nonetheless, ceria features excellent chemical stability, high oxygen storage ability and easy

Table 3
Brief literature review for biochar-based materials applied as ORR electrocatalysts hydrogen fuel cells. (CeO_2/BC: ceria on biochar carbon, Fe-N-$C_{CO2\text{-}tea}$: iron and nitrogen co-doped carbon with pyrolyzed waste tea activated by CO_2, BC-Ce-2: ceria-encapsulated nitrogen-doped biochar, FeN@C-1%: Iron-nitrogen encapsulated in the N-doped biochar, Co@NC_{BC}: Co-loaded N-doped biochar, Treated PP-NS-600-Ta-900: N-S-Ta co-doped pomelo peel biomass, $S^{-}_{1/20}$-OZC-800: fresh herb residue activated with $ZnCl_2$ and mixed with thiourea.)

Material	Onset Potential	Transferred Electrons	Reference
CeO_2/BC	0.79V	3.9 @0.5V	[55]
Fe-N-$C_{CO2\text{-}tea}$	0.95V	3.9 @0.8V	[8]
BC-Ce-2	0.9V	3.55 @0.5V	[56]
FeN@C-1%	0.93V	3.9 @0.6V	[57]
Co@NC_{BC}	0.98V	3.95 @0.8V	[58]
Treated PP-NS-600-Ta-900	0.94V	3.85 @0.4V	[59]
$S^{-}_{1/20}$-OZC-800	0.94 V	3.5 @0.5V	[60]
Sn@dCNC	0.68V	3.8 @0.4V	Present work

electron transfer are counterbalanced by a high cost and an elevate toxicity. For these reasons, according to our opinion, it could be better to use tin oxide as functionalizing metal oxide, favoring the easy handling even at the expense of catalytic activity losses. Zago et al. [8] reported another interesting case of study but it has to be noticed that iron (II) phthalocyanine was introduced by mechano-chemical route through ball milling into the carbon skeleton, implying a less green and cheap synthesis. Other transition metals tailored biochar, like cobalt or tantalum [58,59] has achieved superior catalytic performances but contrary to the present work they were considerably more toxic and hard to manage. Accordingly, Sn@d-CNC paves the way in the improvement of the design of alternative electrocatalysts for the oxygen reduction reaction at cathodes of fuel cells, keeping the costs cheap and the synthesis green.

5. Conclusions

In this work we proposed an interesting nanocomposite based on conductive CNC and tin oxide as promising candidate as low-cost catalyst for ORR. We demonstrated both the possibility to easy recover conductive materials from biomass as ideal catalytic substrate and to activate them via a modern green and fast microwave process, that can be a reliable alternative to time consuming traditional hydrothermal routes. The resulting surface functionalization of CNCs with tin oxide nanocrystals and carbon lattice co-doping showed excellent electrochemical properties. It was also possible to put in evidence that the introduction of co-doping in carbon lattice creates additional active centers for a better absorption of oxygen molecules without any competition with the catalytic behavior of tin oxide NCs dispersed on the CNC surface. On the contrary, the electrochemical cooperation between the co-doping and the SnO_2 nanocrystals decoration leads to good performances of Sn@dCNC material towards the ORR, witnessing this work as a successful example for the design of low-cost and effective electrocatalysts. The interesting findings suggest promising potential of implementing the biochar-based material in alkaline fuel cells and metal-air batteries.

CRediT authorship contribution statement

Giulia Gianola: Methodology, Validation, Formal analysis, Investigation, Data curation, Writing – original draft, Writing – review & editing. **Nadia Garino:** Conceptualization, Methodology, Validation, Formal analysis, Investigation, Data curation, Writing – original draft, Writing – review & editing, Supervision. **Mattia Bartoli:** Conceptualization, Methodology, Formal analysis, Investigation, Data curation, Writing – original draft, Writing – review & editing, Supervision. **Adriano Sacco:** Methodology, Validation, Formal analysis, Investigation, Data curation, Writing – original draft, Writing – review & editing. **Candido F. Pirri:** Investigation, Resources, Writing – original draft, Writing – review & editing, Supervision, Project administration, Funding acquisition. **Juqin Zeng:** Methodology, Validation, Formal analysis, Investigation, Data curation, Writing – original draft, Writing – review & editing.

Declaration of competing interest

The authors declare that they have no known competing financial interests or personal relationships that could have appeared to influence the work reported in this paper.

Data availability

Data will be made available on request.

Appendix A. Supplementary data

Supplementary data to this article can be found online at https://doi.org/10.1016/j.matchemphys.2023.128205.

References

[1] V. Masson-Delmotte, P. Zhai, A. Pirani, S.L. Connors, C. Péan, S. Berger, N. Caud, Y. Chen, L. Goldfarb, M. Gomis, Climate Change 2021: the Physical Science Basis, Contribution of Working Group I to the Sixth Assessment Report of the Intergovernmental Panel on Climate Change, vol. 2, 2021.

[2] O.Z. Sharaf, M.F. Orhan, An overview of fuel cell technology: fundamentals and applications, Renew. Sustain. Energy Rev. 32 (2014) 810–853.

[3] J.S. Lee, S. Tai Kim, R. Cao, N.S. Choi, M. Liu, K.T. Lee, J. Cho, Metal–air batteries with high energy density: Li–air versus Zn–air, Adv. Energy Mater. 1 (2011) 34–50.

[4] S. Li, Y. Hu, Q. Xu, J. Sun, B. Hou, Y. Zhang, Iron-and nitrogen-functionalized graphene as a non-precious metal catalyst for enhanced oxygen reduction in an air-cathode microbial fuel cell, J. Power Sources 213 (2012) 265–269.

[5] K. Nagasawa, S. Takao, K. Higashi, S.-i. Nagamatsu, G. Samjeské, Y. Imaizumi, O. Sekizawa, T. Yamamoto, T. Uruga, Y. Iwasawa, Performance and durability of Pt/C cathode catalysts with different kinds of carbons for polymer electrolyte fuel cells characterized by electrochemical and in situ XAFS techniques, Phys. Chem. Chem. Phys. 16 (2014) 10075–10087.

[6] Y. Gorlin, C.-J. Chung, D. Nordlund, B.M. Clemens, T.F. Jaramillo, Mn_3O_4 supported on glassy carbon: an active non-precious metal catalyst for the oxygen reduction reaction, ACS Catal. 2 (2012) 2687–2694.

[7] A. Sacco, N. Garino, A. Lamberti, C.F. Pirri, M. Quaglio, Anodically-grown TiO_2 nanotubes: effect of the crystallization on the catalytic activity toward the oxygen reduction reaction, Appl. Surf. Sci. 412 (2017) 447–454.

[8] S. Zago, M. Bartoli, M. Muhyuddin, G.M. Vanacore, P. Jagdale, A. Tagliaferro, C. Santoro, S. Specchia, Engineered biochar derived from pyrolyzed waste tea as a carbon support for Fe-NC electrocatalysts for the oxygen reduction reaction, Electrochim. Acta (2022), 140128.

[9] Q. Lv, W. Si, J. He, L. Sun, C. Zhang, N. Wang, Z. Yang, X. Li, X. Wang, W. Deng, Selectively nitrogen-doped carbon materials as superior metal-free catalysts for oxygen reduction, Nat. Commun. 9 (2018) 1–11.

[10] J. Quílez-Bermejo, E. Morallón, D. Cazorla-Amorós, Metal-free heteroatom-doped carbon-based catalysts for ORR: a critical assessment about the role of heteroatoms, Carbon 165 (2020) 434–454.

[11] D.J. You, K. Kwon, C. Pak, H. Chang, Platinum–antimony tin oxide nanoparticle as cathode catalyst for direct methanol fuel cell, Catal. Today 146 (2009) 15–19.

[12] N. Garino, A. Sacco, M. Castellino, J.A. Muñoz-Tabares, M. Armandi, A. Chiodoni, C.F. Pirri, One-pot microwave-assisted synthesis of reduced graphene oxide/iron oxide nanocomposite catalyst for the oxygen reduction reaction, ChemistrySelect 1 (2016) 3640–3646.

[13] N. Garino, A. Sacco, A. Chiodoni, C.F. Pirri, M. Castellino, Microwave-assisted synthesis of nitrogen and sulphur doped graphene decorated with antimony oxide: an effective catalyst for oxygen reduction reaction, Materials 15 (2022) 10.

[14] L. Ai, T. Tian, J. Jiang, Ultrathin graphene layers encapsulating nickel nanoparticles derived metal–organic frameworks for highly efficient electrocatalytic hydrogen and oxygen evolution reactions, ACS Sustain. Chem. Eng. 5 (2017) 4771–4777.

[15] C.O. Tuck, E. Pérez, I.T. Horváth, R.A. Sheldon, M. Poliakoff, Valorization of biomass: deriving more value from waste, Science 337 (2012) 695–699.

[16] A. Jain, S. Sarsaiya, M.K. Awasthi, R. Singh, R. Rajput, U.C. Mishra, J. Chen, J. Shi, Bioenergy and bio-products from bio-waste and its associated modern circular economy: current research trends, challenges, and future outlooks, Fuel 307 (2022), 121859.

[17] M. Bartoli, M. Giorcelli, P. Jagdale, M. Rovere, A. Tagliaferro, A review of non-soil biochar applications, Materials 13 (2020) 291–296.

[18] J. Deng, M. Li, Y. Wang, Biomass-derived carbon: synthesis and applications in energy storage and conversion, Green Chem. 18 (2016) 4824–4854.

[19] S. Tabac, D. Eisenberg, Pyrolyze this paper: can biomass become a source for precise carbon electrodes? Current Opinion in Electrochemistry 25 (2021), 100638.

[20] M. Borghei, N. Laocharoen, E. Kibena-Põldsepp, L.-S. Johansson, J. Campbell, E. Kauppinen, K. Tammeveski, O.J. Rojas, N. Porous, P-doped carbon from coconut shells with high electrocatalytic activity for oxygen reduction: alternative to Pt-C for alkaline fuel cells, Appl. Catal. B Environ. 204 (2017) 394–402.

[21] D. Trache, M.H. Hussin, M.M. Haafiz, V.K. Thakur, Recent progress in cellulose nanocrystals: sources and production, Nanoscale 9 (2017) 1763–1786.

[22] M.S. Smole, S. Hribernik, M. Kurečič, A.U. Krajnc, T. Kreže, K.S. Kleinschek, Surface Properties of Non-conventional Cellulose Fibres, Springer, 2019.

[23] D.V. Cuong, B.M. Matsagar, M. Lee, M.S.A. Hossain, Y. Yamauchi, M. Vithanage, B. Sarkar, Y.S. Ok, K.C.-W. Wu, C.-H. Hou, A critical review on biochar-based engineered hierarchical porous carbon for capacitive charge storage, Renew. Sustain. Energy Rev. 145 (2021), 111029.

[24] C.d.M.S. Rios, V. Simone, L. Simonin, S. Martinet, C. Dupont, Biochars from various biomass types as precursors for hard carbon anodes in sodium-ion batteries, Biomass Bioenergy 117 (2018) 32–37.

[25] X. Li, J. Zhang, B. Liu, Z. Su, A critical review on the application and recent developments of post-modified biochar in supercapacitors, J. Clean. Prod. 310 (2021), 127428.

[26] N. Jafri, W. Wong, V. Doshi, L. Yoon, K.H. Cheah, A review on production and characterization of biochars for application in direct carbon fuel cells, Process Saf. Environ. Protect. 118 (2018) 152–166.

[27] M. Bartoli, M. Giorcelli, M. Rovere, P. Jagdale, A. Tagliaferro, M. Chae, D. C. Bressler, Shape tunability of carbonized cellulose nanocrystals, SN Appl. Sci. 1 (2019) 1661–1676.

[28] R. Arrigo, M. Bartoli, D. Torsello, G. Ghigo, G. Malucelli, Thermal, dynamic-mechanical and electrical properties of UV-LED curable coatings containing porcupine-like carbon structures, Mater. Today Commun. 28 (2021), 102630.

[29] Y. Habibi, L.A. Lucia, O.J. Rojas, Cellulose nanocrystals: chemistry, self-assembly, and applications, Chem. Rev. 110 (2010) 3479–3500.

[30] H.S. Kim, M.A. Abbas, M.S. Kang, H. Kyung, J.H. Bang, W.C. Yoo, Study of the structure-properties relations of carbon spheres affecting electrochemical performances of EDLCs, Electrochim. Acta 304 (2019) 210–220.

[31] S. Huang, Y. Meng, Y. Cao, S. He, X. Li, S. Tong, M. Wu, N-, O- and P-doped hollow carbons: metal-free bifunctional electrocatalysts for hydrogen evolution and oxygen reduction reactions, Appl. Catal. B Environ. 248 (2019) 239–248.

[32] A. Camisasca, A. Sacco, R. Brescia, S. Giordani, Boron/nitrogen-codoped carbon nano-onion electrocatalysts for the oxygen reduction reaction, ACS Appl. Nano Mater. 1 (2018) 5763–5773.

[33] X. Chen, X. Xu, Z. Yang, Z. Liu, L. Zhang, X. Xu, Y. Chen, S. Huang, Sulfur-doped porous reduced graphene oxide hollow nanosphere frameworks as metal-free electrocatalysts for oxygen reduction reaction and as supercapacitor electrode materials, Nanoscale 6 (2014) 13740–13747.

[34] J. Zhang, J. Zhang, F. He, Y. Chen, J. Zhu, D. Wang, S. Mu, H.Y. Yang, Defect and doping Co-engineered non-metal nanocarbon ORR electrocatalyst, Nano-Micro Lett. 13 (2021) 65.

[35] M.A. Hoque, D.C. Higgins, F.M. Hassan, J.-Y. Choi, M.D. Pritzker, Z. Chen, Tin oxide-mesoporous carbon composites as platinum catalyst supports for ethanol oxidation and oxygen reduction, Electrochim. Acta 121 (2014) 421–427.

[36] V. Avila-Vazquez, M. Galvan-Valencia, J. Ledesma-Garcia, L. Arriaga, V. Collins-Martinez, C. Guzman-Martinez, I. Escalante-Garcia, S. Duron-Torres, Electrochemical performance of a Sb-doped SnO2 support synthesized by coprecipitation for oxygen reactions, J. Appl. Electrochem. 45 (2015) 1175–1185.

[37] N. Garino, A. Sacco, M. Castellino, J.A. Munñoz-Tabares, A. Chiodoni, V. Agostino, V. Margaria, M. Gerosa, G. Massaglia, M. Quaglio, Microwave-assisted synthesis of reduced graphene oxide/SnO2 nanocomposite for oxygen reduction reaction in microbial fuel cells, ACS Appl. Mater. Interfaces 8 (2016) 4633–4643.

[38] M. Giorcelli, M. Bartoli, A. Sanginario, E. Padovano, C. Rosso, M. Rovere, A. Tagliaferro, High-temperature annealed biochar as a conductive filler for the production of piezoresistive materials for energy conversion application, ACS Applied Electronic Materials 3 (2021) 838–844.

[39] A. Tagliaferro, M. Rovere, E. Padovano, M. Bartoli, M. Giorcelli, Introducing the novel mixed Gaussian-lorentzian lineshape in the analysis of the Raman signal of biochar, Nanomaterials 10 (2020) 1748.

[40] N. Garino, M. Castellino, A. Sacco, F. Risplendi, J.A. Muñoz-Tabares, M. Armandi, A. Chiodoni, D. Salomon, M. Quaglio, C.F. Pirri, Proving the existence of Mn porphyrin-like complexes hosted in reduced graphene oxide with outstanding performance as oxygen reduction reaction catalysts, 2D Mater. 6 (2019), 045001.

[41] O.M. Vanderfleet, E.D. Cranston, Production routes to tailor the performance of cellulose nanocrystals, Nat. Rev. Mater. 6 (2021) 124–144.

[42] D. Beyene, M. Chae, J. Dai, C. Danumah, F. Tosto, A.G. Demesa, D.C. Bressler, Characterization of cellulase-treated fibers and resulting cellulose nanocrystals generated through acid hydrolysis, Materials 11 (2018) 1272.

[43] A. Orlando, F. Franceschini, C. Muscas, S. Pidkova, M. Bartoli, M. Rovere, A. Tagliaferro, A comprehensive review on Raman spectroscopy applications, Chemosensors 9 (2021) 262.

[44] F. Tuinstra, J.L. Koenig, Raman spectrum of graphite, J. Chem. Phys. 53 (1970) 1126–1130.

[45] A.C. Ferrari, J. Robertson, Interpretation of Raman spectra of disordered and amorphous carbon, Phys. Rev. B 61 (2000), 14095.

[46] A.C. Ferrari, J. Robertson, A.C. Ferrari, J. Robertson, Raman spectroscopy of amorphous, nanostructured, diamond like carbon, and nanodiamond, Philos. Trans. R. Soc. London, Ser. A: Math. Phys. Eng. Sci. 362 (2004) 2477–2512.

[47] A. Shen, Y. Zou, Q. Wang, R.A. Dryfe, X. Huang, S. Dou, L. Dai, S. Wang, Oxygen reduction reaction in a droplet on graphite: direct evidence that the edge is more active than the basal plane, Angew. Chem. 126 (2014) 10980–10984.

[48] X. Yan, Y. Jia, X. Yao, Defects on carbons for electrocatalytic oxygen reduction, Chem. Soc. Rev. 47 (2018) 7628–7658.

[49] S. Ravi, S. Zhang, Y.-R. Lee, K.-K. Kang, J.-M. Kim, J.-W. Ahn, W.-S. Ahn, EDTA-functionalized KCC-1 and KIT-6 mesoporous silicas for Nd^{3+} ion recovery from aqueous solutions, J. Ind. Eng. Chem. 67 (2018) 210–218.

[50] S. Sahu, P. Rani Sahoo, S. Patel, B. Mishra, Oxidation of thiourea and substituted thioureas: a review, J. Sulfur Chem. 32 (2011) 171–197.

[51] S. Kabir, K. Artyushkova, A. Serov, P. Atanassov, Role of nitrogen moieties in N-doped 3D-graphene nanosheets for oxygen electroreduction in acidic and alkaline media, ACS Appl. Mater. Interfaces 10 (2018) 11623–11632.

[52] E.C. Greyson, J.E. Barton, T.W. Odom, Tetrahedral zinc blende tin sulfide nano-and microcrystals, Small 2 (2006) 368–371.

[53] A.K. Mishra, S. Ramaprabhu, Carbon dioxide adsorption in graphene sheets, AIP Adv. 1 (2011), 032152.

[54] G. Wu, K.L. More, C.M. Johnston, P. Zelenay, High-performance Electrocatalysts for Oxygen Reduction Derived from Polyaniline, Iron, and Cobalt, 2011, pp. 443–448.

[55] N. Bhuvanendra, S. Ravichandran, S. Kandasamy, W. Zhang, Q. Xu, L. Khotseng, T. Maiyalagan, H. Su, Spindle-shaped CeO$_2$/biochar carbon with oxygen-vacancy as an effective and highly durable electrocatalyst for oxygen reduction reaction, Int. J. Hydrogen Energy 46 (2021) 2128–2142.

[56] L. Pi, R. Jiang, W. Cai, L. Wang, Y. Wang, J. Cai, X. Mao, Bionic preparation of CeO$_2$-encapsulated nitrogen self-doped biochars for highly efficient oxygen reduction, Applied Material and Interfaces 12 (2020) 3642–3653.

[57] H. Kuo, Y. Lin, C. Chiang, S. Liu, FeN@N-doped graphitic biochars derived from hydrothermal-microwave pyrolysis of cellulose biomass for fuel cell catalysts, Journal of Analytical and Applied Pyrolisis 153 (2021), 104991.

[58] Y. Ye, T. Qian, H. Jiang, Co-loaded N-doped biochar as a high performance oxygen reduction reaction eelectrocatalys by combined pyrolysis of biomass, Ind. Eng. Chem. Res. 59 (2020) 15614–15623.

[59] K. Maliutina, J. Huang, T. Su, J. Yu, L. Fan, Biomass-derived Ta,N,S co-doped CNTs enriched carbon catalyst for efficient electrochemical oxygen reduction, J. Alloys Compd. 8 (2021) 230–235.

[60] H. Yuan, Y. Zhao, J. Yang, C. Xiong, D. Li, N, S-co doping of activated biochar from herb residue for enhanced electrocatalytic performance toward oxygen reduction reaction, Journal of Analytical and Applied Physics 166 (2022), 105606.